

DESIGN, BUILDING, AND TESTING OF SUPERball:
A TENSEGRITY ROBOT TO ENABLE SPACE
EXPLORATION

Jonathan Bruce

March 28, 2016

Table of Contents

List of Figures	3
List of Tables	5
1 Introduction	6
1.1 Motivation	6
1.2 Goals	8
2 Literature Review	9
2.1 Tensegrity Structures	9
2.2 Prior Work in Tensegrity Robotics Design	10
2.3 Tensegrity Robotics for Space Exploration	11
3 Modeling and Model Validation	12
3.1 Euler-Lagrange Model	14
3.2 Detailed Impact Simulations and Cross-Validation Using Two Simulators	16
3.3 Simulated Drop Tests and Payload Protection	18
3.4 Landing Orientation Studies	19
3.5 Conclusions from Simulation Experiments	20
4 Design	22
4.1 Mechanical	23
4.1.1 Spring Holder	23
4.1.2 Battery Holder	23
4.1.3 Motor and Electronics	24
4.1.4 Cable Actuation and Routing	25
4.1.5 Ground Contact	26
4.2 Electrical	26

4.2.1	Motor Board	27
4.2.2	Sensor Board and Beagle Bone Black	27
4.2.3	Power Board	28
4.3	Communication and Power	29
4.3.1	CAN Bus	30
4.3.2	WiFi and the Robot Operating System	30
5	Current and Future Work	32
5.1	SUPERball Current State	32
5.1.1	Dynamic Torque Sensor Testing	32
5.1.2	Global Force Redistribution Sensor Testing	34
5.1.3	Basic Locomotion	34
5.2	Future Work	35
5.2.1	Open Loop Locomotion Control	35
5.2.2	Closed Loop Locomotion Control	35

List of Figures

1.1	<i>Tensegrity structures are composed of pure compression and tension elements. They can be lightweight, reliable, deployable, and efficient to manipulate. Mission Scenario - Tightly packed set of tensegrities, expand, spread out, fall to surface of moon, then safely bounce on impact. The same tensegrity structure which cushioned the landing is then used for mobility to explore moons such as Titan and small asteroids.</i>	6
1.2	Tensegrity Structure. <i>Tensegrities are composed of pure tension and pure compression elements (e.g. cables and rods) as seen in this picture of a tensegrity robot from our physics based tensegrity simulator. They are light-weight, energy-efficient and robust to failures.</i>	7
3.1	SUPERball, fully assembled, in the NASA Ames Research Center Roverscape.	12
3.2	SUPERball with a payload modeled within NTRT.	15
3.3	NTRT vs EL: Vertical Position	17
3.4	NTRT vs EL Vertical Velocity	18
3.5	NTRT vs EL Vertical Acceleration	19
3.6	Landing Forces Study. <i>This shows how rod length impacts maximum deceleration of the payload and the maximum forces experienced by the tension cables. All tests were conducted with a landing velocity of 15 m/s onto a hard surface.</i>	20
3.7	<i>Heat map of the maximum acceleration that the payload encounters for all possible landing orientations. Black areas are safe, colored areas are where the payload does not meet one or both success criteria.</i>	21
4.1	Fully assembled Modular Tensegrity Robot images on SUPERball	22
4.2	Time lapsed stills of spring compression in the MTR spring holder. Note that these stills are from a previous version of the MTR.	24

4.3	Cable routing roller guide within an MTR.	26
4.4	Pictures of each of the main micro-controller boards on an MTR.	29
4.5	This is a connection diagram for power and communication for a MTR on SUPERball.	30
4.6	A simplified representation of how messages are passed within the SUPERball ROS network.	31
5.1	Motor mount torque sensor data and motor position data recorded during a square wave input position trajectory for a single motor. This plot shows measured tension from the sensor and cable length from motor encoder measurements as a function of time for this dynamic movement.	33
5.2	Global force redistribution test. Yellow marks are the means of roughly 5,000 tension sensor measurements of <i>cable 2</i> opposite that which is actuated (<i>cable 1</i>). The black line shows the linear interpolation between points, with the red boundary as standard deviation. The pretension in the sensed cable is adjusted in each test, showing measurement sequences at increasing pretensions.	33
5.3	SUPERball performing a single face-change movement, from one equilateral triangular face to another. The robot begins with all MTRs of the red triangle touching the ground. Then, SUPERball retracts the yellow-highlighted cable on the red triangle, inducing movement. Frame 2 shows SUPERball halfway through the movement with only two points of contact on the ground. Finally, frame 3 shows SUPERball at the end, with all 3 points of the blue triangle in ground contact.	34

List of Tables

3.1	SUPERball and Related Robots Design Overview.	14
4.1	100W Maxon BLDC Motor Parameters	27

Chapter 1

Introduction

The text and ideas presented in this section were originally proposed by the NASA Innovative Advance Concepts (NIAC) solicitation submitted in 2013 and granted in 2014 [1]. My dissertation proposal draws heavily from this project and was funded by this grant.

1.1 Motivation

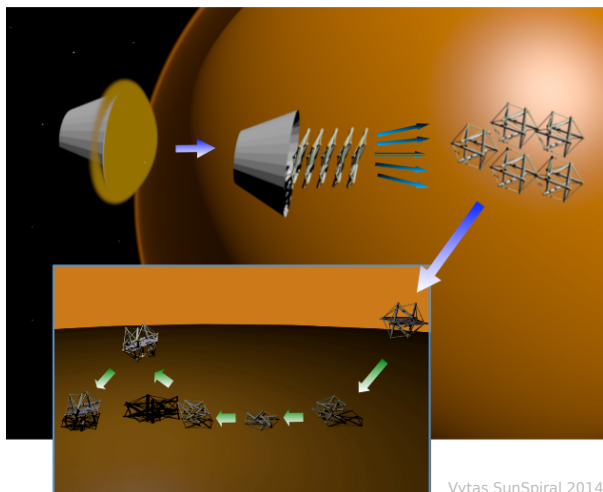


Figure 1.1: Tensegrity structures are composed of pure compression and tension elements. They can be lightweight, reliable, deployable, and efficient to manipulate. **Mission Scenario** - Tightly packed set of tensegrities, expand, spread out, fall to surface of moon, then safely bounce on impact. The same tensegrity structure which cushioned the landing is then used for mobility to explore moons such as Titan and small asteroids.

Tensegrity robots can facilitate an intriguing low-cost planetary exploration mission profile (see Figure 1.1) comprising of the following stages: 1) A set of tensegrity robots can be squeezed into a small launch platform; 2) After initial atmospheric entry and ejection of the heat shield, they can automatically spring away from each other when released at their destination. 3)

They “bounce” on impact reducing the need for final descent equipment, such as airbags; and 4) They can reorient themselves from landed position without addition reorientation hardware and efficiently move from scattered initial positions to perform sensor measurements; 5) They can survive significant falls and are resistant to being stuck, simplifying route planning and allowing for more aggressive exploration in the pursuit of science.

Once on the surface, tensegrity robots can perform an array of scientific analysis including soil and atmospheric composition, surface imagery and microscopic analysis. To further reduce complexity, sensors can be suspended on the interior of the tensegrity on cables attached to the nodes, or when appropriate even to the nodes themselves so that the sensors can be moved with movements of the structure itself, eliminating the need for separate sensor arms. In addition, environmental analysis can be performed in-situ at the landing site, at different local locations, or even at distant locations given a tensegrity robot’s potential for efficient locomotion. The biggest advantages of this mission profile are:

1. The structure of the robot itself provides capability for deployment, landing (EDL), and mobility, reducing complexity, risk, and mass compared to using three separate systems.
2. Tensegrity robots are light-weight and can be packed tightly, reducing cost.
3. Can scale to multiple tightly packed robots to increase scientific coverage and reduce risk.
4. Flexibility and modularity of robot design allows design reuse, reducing mission project risk.

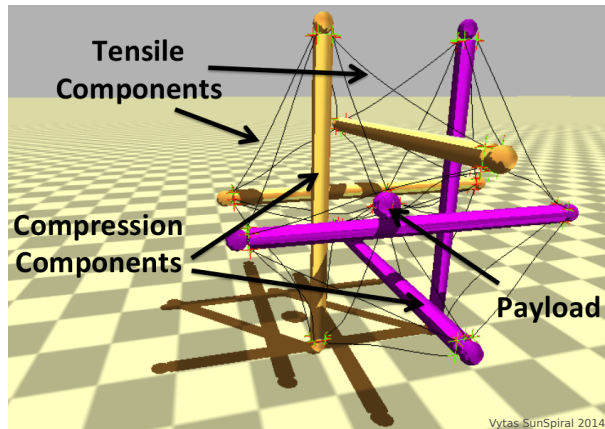


Figure 1.2: Tensegrity Structure. Tensegrities are composed of pure tension and pure compression elements (e.g. cables and rods) as seen in this picture of a tensegrity robot from our physics based tensegrity simulator. They are light-weight, energy-efficient and robust to failures.

1.2 Goals

The main goals my project seeks to accomplish:

1. Build a rolling tensegrity robot

A physical hardware prototype of an untethered tensegrity robot to explore locomotion. The robot will not only need to perform the basics for rolling, but will need to enable the next two goal items. To achieve this, the robot will need significant mechanical power, distributed computation, and wireless communication.

2. Open loop locomotion control

Once the hardware prototype is built, an open loop control scheme will be developed. The open loop algorithm will not change the control inputs to the system based on sensing outside of the robot. This will demonstrate the system's ability to coordinate motion between it's distributed computation and collect data wirelessly.

3. Closed loop "gait" control

Once the system has proven the ability to locomote open loop, a closed loop algorithm will be developed. The closed loop control will change the "gait", or locomotion pattern, of the robot to cope with sensed variations in terrain, e.g. changes in terrain grade or climbing over an obstacles. To achieve this, research into the how much of the robot state is needed as well as various techniques to model and predict the environment by using the on board sensors.

Chapter 2

Literature Review

2.1 Tensegrity Structures

It is possible to design free-standing structures with axially loaded compression elements in a well crafted network of tensional elements. Such an arrangement is called a tensegrity structure (tensile integrity). Each element of the structure experiences either pure axial compression or pure tension [9][23]. The absence of bending or shear forces allows for highly efficient use of materials, resulting in lightweight, yet robust systems.

Because the struts are not directly connected, tensegrities have the unique property that externally applied forces distribute through the structure via multiple load paths. This creates a soft structure, for a soft robot, out of inherently rigid materials. Since there are no rigid connections within the structure, there are also no lever arms to magnify forces. The result is a global level of robustness and tolerance to forces applied from any direction.

This makes tensegrity robots inherently compliant and extremely well suited for physical interactions with complex and poorly modeled natural environments. Active motion in tensegrity robots can be performed by changing cable lengths in parallel, enabling the use of many small actuators that work together, rather than individual heavy actuators which work in series. There are also many indications that tensegrity properties are prevalent throughout biological systems, and the morphology of the SUPERball that we are studying, especially when carrying a payload, ends up bearing a striking resemblance to the nucleated tensegrity model of cell structure [28][27].

2.2 Prior Work in Tensegrity Robotics Design

An important advantage of tensegrity structures with respect to general pin-jointed structures is their increased mass-efficiency due to a high fraction of tensile members. Tensile members are generally more mass-efficient as they do not need to resist buckling. A further advantage from a robotics perspective is that forces diffuse in a tensegrity. There are no lever arms and torques do not accumulate at the joints as in a classic serial manipulator. Forces distribute through multiple load paths, thus increasing robustness and tolerance to mechanical failure.

The static properties of tensegrities have been thoroughly studied and some basic analysis is discussed in section 3. On the other hand, few examples are known of truly dynamic motion of these structures. Early examples of kinematic motion include the work at EPFL’s IMAC laboratory [8]. Skelton and Sultan introduced algorithms for the positioning of tensegrity based telescopes and the dynamic control of a tensegrity flight simulator platform [24]. Although there were some early efforts at MIT’s CSAIL lab, it wasn’t until the work of Paul and Lipson at Cornell University that the concept of tensegrity robotics became widespread [18]. Paul and Lipson were the first to study the properties of dynamic tensegrity structures in hardware and simulation. A few years later Fivat and Lipson designed the IcoTens, a small actuated tensegrity icosahedron robot, but did not publish results. In recent years, the BIER lab at the University of Virginia has been studying Central Pattern Generator based control for tensegrity based fish tails, which is closely related to the control architectures proposed for SUPERball [6, 2]. Mirats-Tur has presented design and controls work on various other tensegrity morphologies that have been tethered or fixed to the ground [10, 17]. At Union College, Rieffel and colleagues are following an interesting line of work by considering vibration based actuation for small tensegrities [12]. Related work was presented by Böhm and Zimmermann, who demonstrated controlled locomotion of vibration driven tensegrity robots with a single actuator [3]. Finally, Shibata, Hirai and colleagues have developed pneumatically actuated rolling tensegrity structures [19].

Building upon these works, the SUPERball project seeks to push forward the tensegrity robotics field and develop truly untethered, highly dynamic and compliant robots exploiting the aforementioned advantages.

2.3 Tensegrity Robotics for Space Exploration

The high strength-to-weight ratio of tensegrity structures is very attractive due to the impact of mass on mission launch costs. Large tensegrity structures have been shown to be deployable from small compact configurations which enable them to fit into space constrained launch fairings. While the above qualities have inspired studies of deployable antennae and other large space structures [26], it is in the realm of planetary exploration that we see the most significant role for many of the unique force distribution qualities of tensegrity robots. The NIAC project currently funding this research [1] specifically studies landing and surface mobility of tensegrities, exploiting the controllable compliance and force distribution properties which make for reliable and robust environmental interactions.

The main goal is to develop tensegrity probes with an actively controllable tensile network to enable compact stowage for launch, followed by deployment in preparation for landing. Due to their natural compliance and structural force distribution properties, tensegrity probes can safely absorb significant impact forces, enabling high speed Entry, Descent, and Landing (EDL) scenarios where the probe itself acts much like an airbag. However, unlike an airbag which must be discarded after a single use, the tensegrity probe can actively control its shape to provide compliant rolling mobility while still maintaining the ability to safely absorb impact shocks that might occur during exploration. This combination of functions from a single structure enables compact and lightweight planetary exploration missions with the capabilities of traditional wheeled rovers, but with a mass and cost similar or less than a stationary probe.

Therefore, a large fraction of the overall weight (as measured at atmospheric entry) of a tensegrity mission can be used for the scientific payload due to the dual use of the structure as a lander and a rover. This allows for cheaper missions and enable new forms of surface exploration that utilize the natural tolerance to impacts of tensegrities [25].

Chapter 3

Modeling and Model Validation



Figure 3.1: SUPERball, fully assembled, in the NASA Ames Research Center Roverscape.

As part of our research for the NASA Innovative Advanced Concepts (NIAC) program, we are developing the SUPERball (Spherical Underactuated Planetary Exploration Robot), which is a compliant icosahedron tensegrity robot designed for planetary landing and exploration, seen in figure 3.1. Tensegrity robots are soft machines which are uniquely able to compliantly absorb forces and interact with unstructured environments. However, instead of engineering a single new robot, we have chosen to develop a fundamentally reusable component for tensegrity robots by creating a modular robotic tensegrity strut which contains an integrated system of power,

sensing, actuation, and communications. The purpose is to enable the exploration of the wide range of possible tensegrity robotic morphologies by simply combining the robotic struts into new systems.

Though there is much prior work in a variety of theoretical areas for tensegrities, engineering knowledge of constructing practical tensegrity robots is limited. Since a staggering variety of different tensegrity structures can be constructed from collections of simple sticks and strings, we have made it a priority to develop self-contained robotic tensegrity struts which can be used to explore and build a wide range of tensegrity robots simply by combining them into novel structures. Our designs are driven by experimental results obtained from a previous prototype, ReCTeR (Reservoir Compliant Tensegrity Robot) in combination with simulation results of our validated tensegrity simulator NTRT (NASA Tensegrity Robotics Toolkit) [7][6].

In order to develop SUPERball from ReCTeR’s design limitations as well as our labs need for rapid experimentation of various tensegrity configurations and morphologies, we came up with a modular tensegrity platform to research large scale robotic tasks; e.g. a tensegrity planetary probe to explore Saturn’s moon Titan. Our lab obtained design requirements through an iterative approach with validated our NTRT simulator by experimental comparison with ReCTeR [6]. We now can quickly evaluate various tensegrity configurations in simulation to find optimal mechanical design goals. In conjunction with the NTRT solver, we also incorporated results obtained with our (open source) Euler Lagrange solver based on Skelton’s work [20] and measurements on ReCTeR. The initial design requirements obtained from the NTRT simulations, refined designs after a first prototype build, and how these compare to other tensegrity robotic systems are given in Table 3.1.

The work presented here is work verifying our in house tensegrity simulators. In order to achieve this, the group decided to use a SUPERball like structure with a center payload. This is believed to be closer to the proposed build profile of a real tensegrity probe, where the main science modules will be contained within the payload. Protecting this science payload is the main goal for and EDL scenario. Figure 3.2 shows a 3-D representation of SUPERball with a payload generated within NTRT.

Table 3.1: SUPERball and Related Robots Design Overview.

	l_{strut}	Δl_{act}	$k_{passive}$	tethered?	control	f_{act}	#act.	mass	sensors	actuators	ref.
Pneumatic	0.57 m	-	-	Y	open loop	800 N	24	3.3 kg	none	McKibben	[14]
ReCTeR	1 m	0.3 m	28.4 N m^{-1}	N	closed loop	12 N	6	1.1 kg	F, L, IMU	DC	[6]
Rapid Proto Kit	0.69 m	0.005 m	1193 N m^{-1}	N	open loop	<45 N	24	2.7 kg	none	linear DC	[13]
SUPERball 2014	1.5 m	0.2 m	613 N m^{-1}	N	closed loop	140 N	12	12 kg	F, L, τ , IMU	BLDC	
SUPERball 2015	1.7 m	0.42 m	998 N m^{-1}	N	closed loop	250 N	12	21 kg	F, L, τ , IMU	BLDC	

The variable l_{strut} indicates the length of a strut, Δl_{act} is the nominal spring-cable retraction length in tension, $k_{passive}$ is the linear stiffness coefficient of a passive spring-cable (or active spring-cable if fully actuated), tethered indicates if the robot is powered externally or by internal systems, control indicates whether sensor feedback is used, f_{act} is the nominal actuated spring-cable tension and #act. is the number of actuators. In the sensors column, F represents a linear force sensor (for cables), L is cable length sensor (in the form of motor encoders), τ represents a torque sensor for motors, and IMU represents an accelerometer/gyroscope inertial motion sensing unit. Actuators are specified as DC motors or brushless DC (BLDC) motors. The SUPERball 2014 values are revised original design requirements based on NTRT simulations, and changed to the 2015 values after additional detail design.

3.1 Euler-Lagrange Model

In order to verify the simulation results produced by our NTRT simulator, we decided to compare the behavior of the NTRT to a published analytic model for tensegrity systems. We choose to use Skelton's dynamic equations because it is a well accepted and used model. It may be found in his *Tensegrity Systems* book [21] which is based on his work in [22]. In order to solve the dynamic equations with interactions with the environment, an Euler-Lagrange approach is used as well as Skelton's constrained class one structure. The lagrange equation for a constrained rod is given by

$$L = T - V - c \quad (3.1)$$

where

$$\mathbf{b} = l^{-1}(\mathbf{n}_j - \mathbf{n}_i) \quad (3.2)$$

$$c = \frac{\mathbf{J}\xi}{2}(\mathbf{b}^T \mathbf{b} - 1) \quad (3.3)$$

Equation (3.2) is the normalized vector of a rod with $\mathbf{n}_{i,j}$ the nodal positions in R^3 , and equation (3.3) contains the lagrange multiplier ξ to keep (3.2) constrained. \mathbf{J} is also defined as the inertia matrix for a one dimensional rod in three dimensional space. In order to define the system of k rods we need to define a combined Lagrangian as

$$\mathbf{L} = \sum_{i=1}^k L_i \quad (3.4)$$

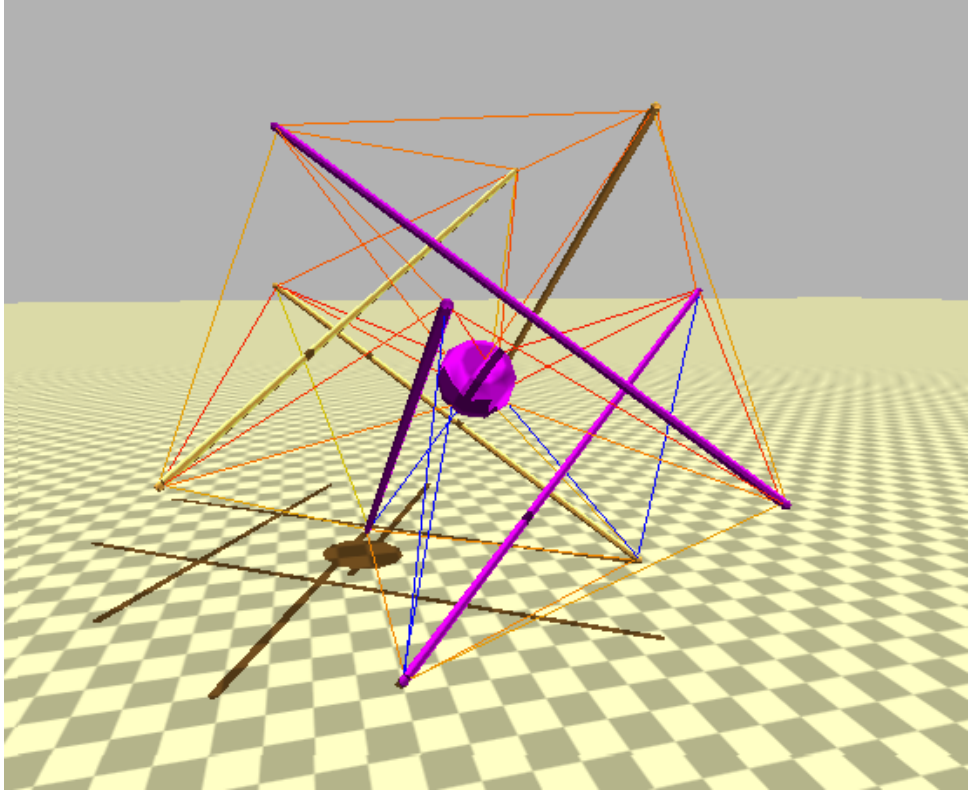


Figure 3.2: SUPERball with a payload modeled within NTRT.

where L_i is the Lagrange function for each rod. Using the approach outlined in Skelton's book for deriving the equations of motion, we can then derive the configuration matrix

$$\mathbf{Q} = \begin{bmatrix} \mathbf{R} & \mathbf{B} \end{bmatrix} \quad (3.5)$$

where \mathbf{R} and \mathbf{B} are matrices containing the translational and rotational vectors, respectively. They have the form

$$\mathbf{R} = \begin{bmatrix} \mathbf{r}_1 & \cdots & \mathbf{r}_k \end{bmatrix} \quad (3.6)$$

$$\mathbf{B} = \begin{bmatrix} \mathbf{b}_1 & \cdots & \mathbf{b}_k \end{bmatrix} \quad (3.7)$$

Also using the procedure to derive generalized forces within Skelton's book, the system's generalized force equations are computed as

$$\mathbf{F}_{\mathbf{Q}} = \begin{bmatrix} \mathbf{F}_{\mathbf{R}} & \mathbf{F}_{\mathbf{B}} \end{bmatrix} \quad (3.8)$$

with

$$\mathbf{F}_R = \begin{bmatrix} \mathbf{f}_{r_1} & \cdots & \mathbf{f}_{r_k} \end{bmatrix} \quad (3.9)$$

$$\mathbf{F}_B = \begin{bmatrix} \mathbf{f}_{b_1} & \cdots & \mathbf{f}_{b_k} \end{bmatrix} \quad (3.10)$$

Finally, we can define the resulting equations of motion in a compact form as

$$(\ddot{\mathbf{Q}} + \mathbf{Q}\boldsymbol{\Xi})\mathbf{M} = \mathbf{F}_Q \quad (3.11)$$

where

$$\boldsymbol{\Xi} = \text{diag} \begin{bmatrix} 0, \dots, 0, \xi_1, \dots, \xi_k \end{bmatrix} \quad (3.12)$$

$$\mathbf{M} = \text{diag} \begin{bmatrix} m_1, \dots, m_k, J_1, \dots, J_k \end{bmatrix} \quad (3.13)$$

This approach was then implemented in Python utilizing a 4th order Runge-Kutta formula for solving the system of ordinary differential equations. In order to implement a gravitational field, a force distribution function is applied along the length of each rod and calculated as a nodal force depending on the given density of the rod. This external force is then applied to the nodes during each time step, simulating a gravitational field.

3.2 Detailed Impact Simulations and Cross-Validation Using Two Simulators

The NTRT simulator is the most general purpose, allowing us to explore control algorithms and complex environmental interactions, but it is an iterative discrete solver that we were concerned might not be providing accurate answers. The E-L solver, on the other hand, has a much stronger analytical basis and should provide very accurate answers, but is limited because some of the nodes (rod ends) must be constrained and locked into place. This is unrealistic for the deformation caused during landing, and makes it an inappropriate choice for mobility and controls research. If ground contact forces are incorporated into the E-L solver and code optimization implemented, it could be used in conjunction with a unscented kalman filter for state estimation propagation. This tool could then be used to develop online learning algorithms

for mobility research.

In this section, we compare the NTRT simulator and E-L solver at the moment of impact with the ground. The simulations are compared at the moment of impact with the ground because our implementation of the analytic E-L solver requires select nodes to be constrained. We setup the structure so that it is barely in contact with the ground and is in balance at time equal to 0. In both simulations, we add an initial velocity equal to the terminal velocity of Titan, and compared each vertical trajectory, vertical velocity, and vertical acceleration of the payload. Since the structure's horizontal speed is zero at the beginning and the structure is symmetrical, the payload's horizontal components of position, velocity and acceleration are zero. As it can be seen in the Figures 3.3 and 3.4, both simulators closely match and generate the same results for position and velocity with the error margin close to zero. Comparing the accelerations generated by two simulators (Figure 3.5), it can be seen that there is a bigger difference. The reason behind this difference is the fact that NTRT uses Bullet, which is a discrete time simulator and accelerations are calculated using two point estimations from velocities at the timestep before. Yet, even with these differences in accelerations, our conclusion at the end of the comparison is that both simulators showed the same basic dynamics and their results were close enough that we could move forward using the more general purpose NTRT Simulator for our controls, mobility, and landing experiments.

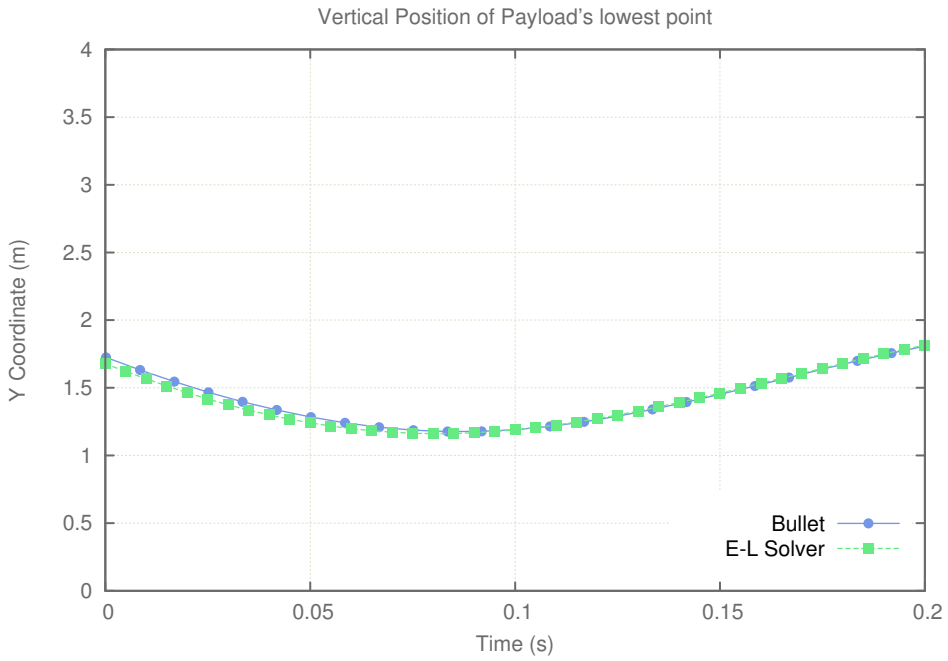


Figure 3.3: NTRT vs EL: Vertical Position

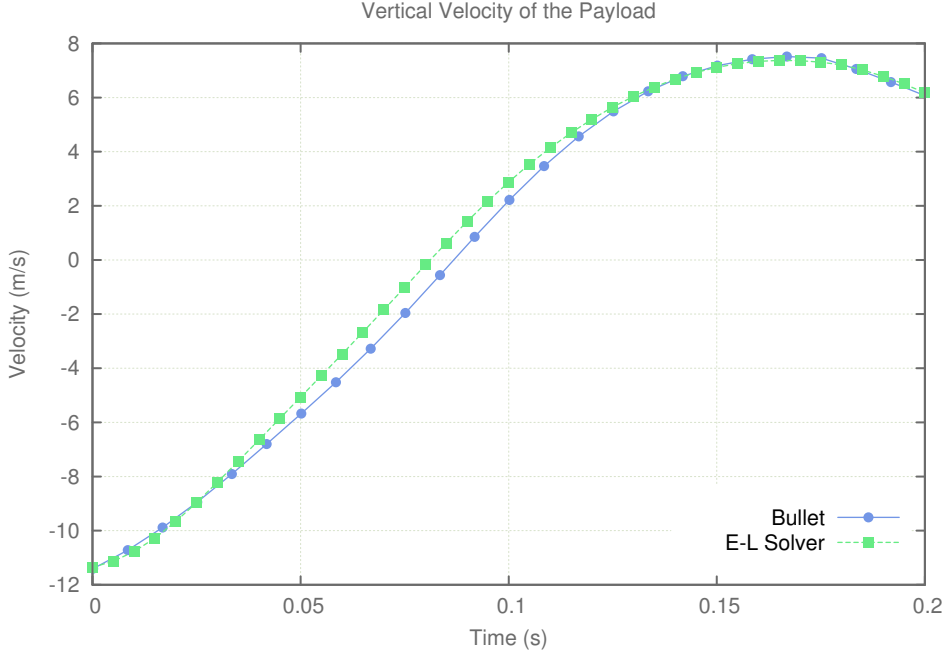


Figure 3.4: NTRT vs EL Vertical Velocity

3.3 Simulated Drop Tests and Payload Protection

Finally, we performed extensive analysis on drop tests and the protection provided to a payload. As expected, we found that by varying the rod lengths, which impacts the stroke distance for the payload to decelerate, we could control the maximum deceleration experienced by the payload while ensuring that it did not collide with the ground or structure. For example, with rods of 1.5 meters in length, our payload experienced a max deceleration of 21.4G when landing at 15 m/s. In figure 3.6 we show the results of a series of drop tests with different rod lengths and show the resulting maximum deceleration and forces experienced in the tension members. As can be seen from these graphs, even for reasonable rod lengths, the maximum G's are acceptable for most instruments, and the maximum forces experienced by the cables are easily within ranges that can be engineered for. In all tests we kept the total system mass constant, at 100kg (which is 70kg for the payload and 5kg per rod) in order to highlight the impact of structural geometry and rod length. For the tension members we used spring constants of 44 kN/m for the cables around the perimeter and 10 kN/m for the cables attached to the payload. Also, the results in Figure 3.6 were found using the landing orientation of 35 degrees around X axis and 45 degrees around Z axis, which we selected from our orientation studies discussed below.

A very interesting point to consider is that the mass of our system will grow in a linear fashion with the length in the rods, while providing increasing payload protection. On the other

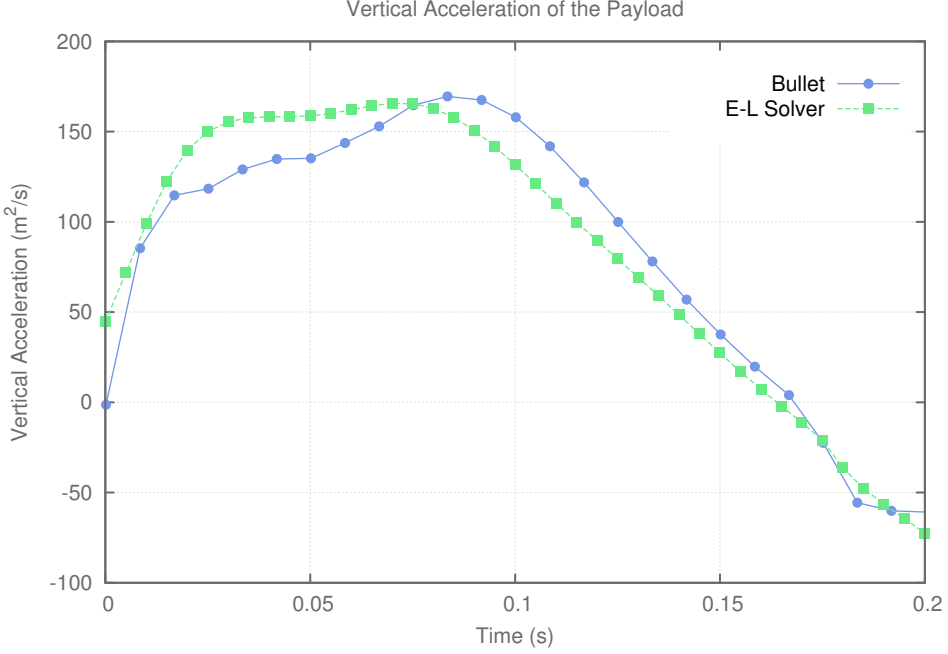


Figure 3.5: NTRT vs EL Vertical Acceleration

hand, the mass of airbags increases with the square of the radius, which is one of the reasons that the MSL rover, with its increased size and mass, had to switch from the airbag approach to the more complex Sky Crane approach. While this study has focused on small light-weight mission concepts, we expect that there are compelling advantages to scaling up to handle larger payloads and we look forward to studying this further in the future.

3.4 Landing Orientation Studies

In order to study how landing orientation affects payload decelerations and impact events, we conducted a systematic study of landing orientations. Since we wanted to get meaningful data, even for bad orientations, we used a larger tensegrity with 4 meter rods so the data wouldn't saturate. Our success criteria for this study was that the decelerations had to stay under an upper limit of 25G deceleration of the payload, and the payload had to avoid collision with the ground or parts of the tensegrity structure. Figure 3.7 shows the orientations that were safely within these criteria (black) or failed one or both of the criteria (colored). By using a simple trailing streamer during descent it would be possible to control landing at an optimal orientation and enable the use of smaller structures with shorter rods because the orientation control would maximize the available stroke for the payload to decelerate within the structure. Conversely, we can use these studies to know what the worst possible landing scenario will be

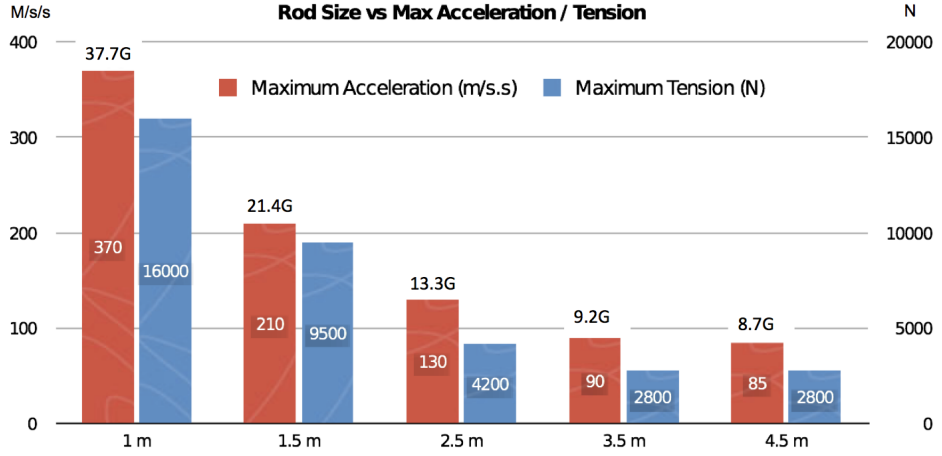


Figure 3.6: **Landing Forces Study.** This shows how rod length impacts maximum deceleration of the payload and the maximum forces experienced by the tension cables. All tests were conducted with a landing velocity of 15 m/s onto a hard surface.

and choose a structure size which will allow safe landing at any orientation.

3.5 Conclusions from Simulation Experiments

In our landing analysis we developed and cross-validated two different simulation methods that allowed us to explore the capabilities of a tensegrity structure to absorb the forces of landing and to simultaneously protect a delicate payload. This analysis confirmed that indeed it is possible to do so using a 6-bar tensegrity probe while maintaining maximum decelerations experienced by the instrument-containing payload to forces less than 25G, despite the structure landing at 15 m/s (which is greater than terminal velocity on Titan). Comparing this to the Huygens probe's landing acceleration of 32G [15], the tensegrity probe will have a 43% reduction in G forces experienced by the scientific payload, despite the Huygens probe's use of parachutes to land at 1/3 of the speed of our tensegrity probe.

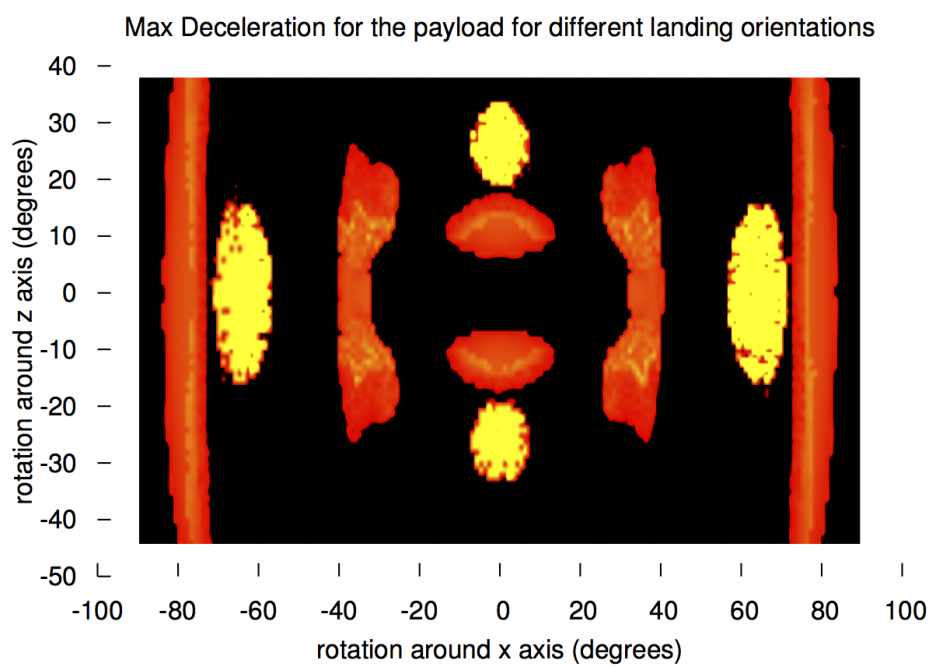
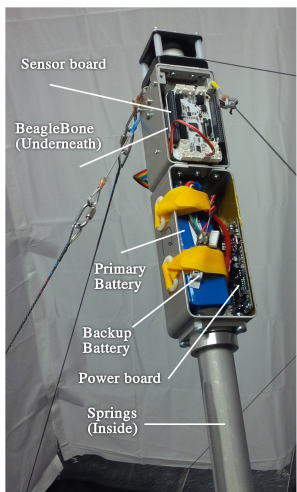


Figure 3.7: Heat map of the maximum acceleration that the payload encounters for all possible landing orientations. Black areas are safe, colored areas are where the payload does not meet one or both success criteria.

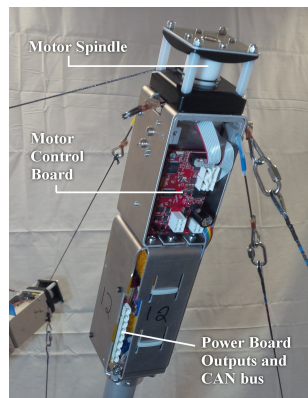
Chapter 4

Design

An ideal tensegrity system, either robotic or static, is a collection of rigid compressible elements suspended within a network of tensioned cables where none of the compressible elements are in direct contact with one another. For robotic tensegrities without a payload, the actuation and supporting electronics would be logically designed into the compressible elements. For the inception of SUPERball, this compressible element called a struct was further dissected into three parts: two identical ends called Modular Tensegrity Robots (MTR) and a section of tube stock connecting the MTRs. Connecting six of these struts into an icosahedron geometric pattern will create SUPERball. Modular Tensgrity Robot is a loose label given to the self-contained robotic element which when connected with multiple MTRs may make up a tensegrity robot. The current version of a MTR can be seen in figure 4.1 and the following subsections will explain the mechanical and electrical make up of an MTR.



(a) MTR front side.



(b) MTR back side.

Figure 4.1: Fully assembled Modular Tensegrity Robot images on SUPERball

4.1 Mechanical

The main structural elements of the MTRs were kept simple to enable each MTR to be self contained so that the MTR may be removed from the connecting rod as one whole unit. The MTRs are held onto the connecting rods by a simple tube collar for easy removal. There are 5 sections to MTR: a spring holder, battery holder, motor and electronics, cable actuation and routing, and a ground contact. Design parameters are shown in table 3.1 in section 3. The supporting metallic structural elements are made from 6061-T6 aluminum and machined plastic elements are Polyoxyethylene (commercially known as Delrin) unless otherwise noted.

4.1.1 Spring Holder

A lesson learned from other tensegrity robots and the designer of ReCTeR [6] was that externally exposed springs are not ideal for a robotic system that would be interacting with a dynamic and unknown environment. The exposed springs get caught on objects and the assumption of near mass-less cables can no longer be applied. On the MTR, an enclosed compression spring system was developed to alleviate these issues. Compression springs were chosen so that during any unknown impact, the springs would not plastically deform. For SUPERball, a spring with a spring constant of $998Nm$ is attached to a passive cable element and a $2850Nm$ spring is attached to an actuated cable. A passive spring was chosen with a total throw of $23cm$ to allow for pretension to be instated into the passive springs as well as to allow a wide dynamic compliant range. Since the actuated cables will be able to dynamically control pretension, a smaller throw spring was chosen to conserve space. Figure 4.2 shows a closeup of how the spring holder functions. How cables are attached to the springs inside the spring holder is explained in section 4.1.4.

4.1.2 Battery Holder

From the inception of SUPERball, enabling a self-contained power source which was easily accessible per MTR was a driving design parameter. During the initial design and build of the SUPERball, it was known that the batteries were to be 24 volt lithium polymer but optimal size and shape of the battery was unknown due to a changing power profile. Therefore, a battery holder with a simple securing mechanism which can handle a wide range of battery sizes was utilized. Two hook and loop straps were used with simple slot cutouts to enable cinching around



Figure 4.2: Time lapsed stills of spring compression in the MTR spring holder. Note that these stills are from a previous version of the MTR.

a generic lithium polymer battery. The holder was also made large enough to hold the Power Board PCB board opposite of the battery. As shown in section 4.2.3, the Power Board was designed to be a low profile to allow for a large battery within the holder.

4.1.3 Motor and Electronics

This section of the MTR used on SUPERball was mechanically designed around the Maxon EC-22 100 watt BLDC motor used for actuation. Each Maxon motor is 22mm in diameter and 108mm long with gearbox and encoder. The output shaft is a 6mm diameter D shaft of length 10.2mm. A size requirement for how large the cross sectional diameter of the MTR could be was a limiting factor in designing the motor and electronic section. The maximum diameter for any section used in the MTR was maximally limited to double the diameter of the connecting rod. The idea for such a limitation was to keep the effective moment arm out from the center axis of any rod to a minimum. Due to the spring size and the need for a spring holder tube, the minimum diameter for the connecting rod was 35mm giving a maximum MTR diameter of 70mm.

The main component in the motor and electronic section of the MTR is the cable routing

support bracket. This bracket plays three roles in the mechanical design: static support for the motor, support for the supporting material, and main exit support for the internal cable routing. Figure 4.3 shows the cable routing support bracket above the pulley. The actual motor mount was designed to be mechanically floating to enable torque sensing directly on the motor mount. Thus, the cable routing support bracket sinks the reaction torque induced by the motor. There are two electronic boards, the Sensor and Motor boards, which are mounted to brackets that straddle the motor. Due to space limitations, these brackets are also load bearing components for the torsional forces induced by the motor.

4.1.4 Cable Actuation and Routing

A simple spool design was implemented to directly actuate the cable. The spool directly couples to the motor shaft by sliding onto the D shaft. A radial bearing supports the top of the spool and since the force vector applied to the spool by the actuated cable will never be just perpendicular to the spool, a thrust bearing was embedded into the bottom of the spool. The thrust bearing sinks the trust force into the motor mount and each spool has the ability to slide along the the shaft's main axis. Since this thrust force is perpendicular to the torque of the motor, this force is not induced into the torque sensor built into the motor mount.

There are three other cables that connect to a MTR on SUPERball, though the device may support more with slight additions not explained here. The cables used externally from the MTR are composed of Vectran braided cable and the cables used within the MTR are braided steel cabling. Two cables are routed through the MTR to the spring housing section and the other is terminated on the outside of the MTR. Both routed cables enter the MTR through the cable routing support bracket mentioned in 4.1.3. The cables are immediately routed around a rolling guide bearing to induce an approximate 90 degree bend to guide the cables towards the spring tube holder section, seen in figure 4.3. After the rolling guide bearing, the cables enter a PTFE tube to create a bowden cable to help route the cables around components within the MTR. Once the cables reach their respective spring within the spring tube holder, the PTFE tube is terminated and the cable is routed through the spring and terminated using a copper compression sleeve.

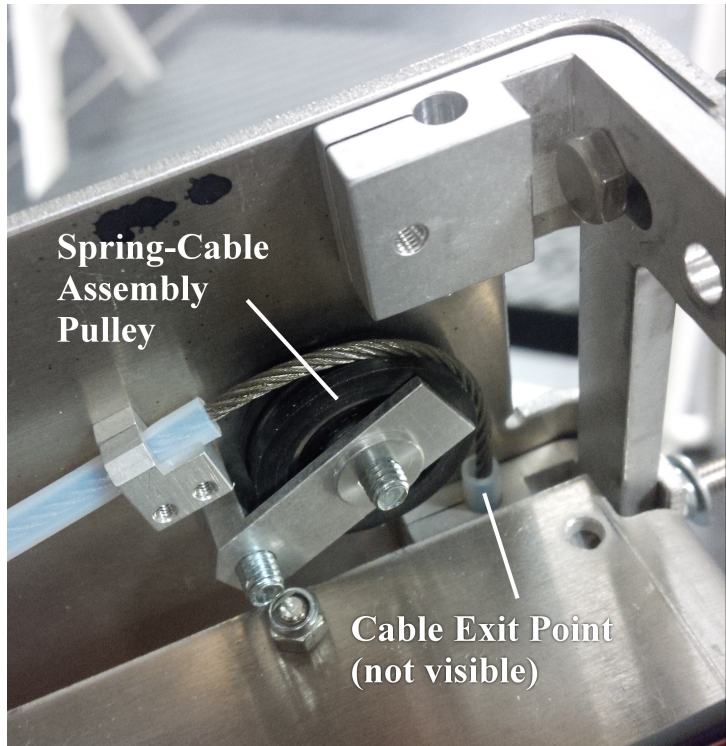


Figure 4.3: Cable routing roller guide within an MTR.

4.1.5 Ground Contact

This final section of the MTR is the simplest. To protect the MTR during locomotion, a 3D printed cap was manufactured to cover the end. This part is designed with a diameter of 80mm so that it is the only part of the MTR that contacts the ground during normal locomotion. To decrease the impact shocks as the rod contacts a surface, compliant foam sheets are placed between the 3D printed cap and the MTR.

4.2 Electrical

SUPERball's electronics were developed with a focus on reliability, safety, and enabling distributed controls. Another parameter was the ability to drive the 100W BLDC Maxon motors. These main design criteria gave way to implement separate electronic boards based on their main function. Each MTR has three custom Microchip dsPIC33e enabled PCB boards and the ability to house one ARM based computer called a Beagle Bone Black. Each custom PCB is designed for very different purposes: A board to condition sensor data and run real-time control loops, a board to condition and distribute a 5.5V electronic power rail and a 24V motor power rail, and a board to control the 100W BLDC motor. The only requirements for each custom

Table 4.1: 100W Maxon BLDC Motor Parameters

Motor without Gearbox				
Nominal Voltage (V)	No Load Speed (rpm)	No Load Current (mA)	Stall Torque (mNm)	Max Efficiency (%)
24	26,500	16.8	691	92
Gearbox				
Reduction	Number of Stages	Max Continuous Torque (Nm)		Max Efficiency (%)
109:1	3	3		59

board is full CAN bus communication support and power conditioning for the 5.5V power rail. The boards are simply named by their main purpose, thus Sensor, Power, and Motor respectively. Though each MTR can house a Beagle Bone Black, SUPERball only has one per strut for cost saving and initial implementation simplicity.

4.2.1 Motor Board

An initial driving parameter used during the design of SUPERball was the BLDC motor. During the design review for SUPERball, a lightweight motor with high power and efficiency was desired. Thus, a Maxon brushless motor was a logical choice. Table 4.1 shows the electrical properties of this motor. In order to effectively drive this motor, a dedicated motor board was used on each MTR. The main development of this board was engineered by Pavlo Manovi, and certain aspects of the board were tailored for our needs [16]. The main components on the Motor board are the Microchip's 16-bit dsPIC33ep256mu506 micro-controller and the Texas Instruments DRV8303 three phase pre-driver. Figure 4.4a shows the current version of the motor board.

4.2.2 Sensor Board and Beagle Bone Black

The sensor board was originally designed as the main processing unit on a MTR. However, the design and building process has lead to the coupling of the sensor board with a Beagle Bone Black. For a detailed explanation of why the Beagle Bone Black was integrated into the system, please refer to 4.3.

The current version of the sensor board was developed as a daughter board for the Beagle Bone Black. The board mates to the Beagle Bone Black through two double row 46 pin headers and provides power and CAN communication to the ARM board. The main processing unit on the sensor board is Microchip's 16-bit dsPIC33ep128gp506 micro-controller. Environmental

sensing is enabled by a 9DOF inertial measurement unit (IMU) and a 24-bit analog to digital converter (ADC) configured in a half wheat-stone bridge configuration. The IMU is comprised of Invensense's MPU6000 mastered to Freescale's MAG3110 magnetometer, and the ADC is Analog Device's AD7193.

The Beagle Bone Black is a open-source hardware single-board computer inspired by the BeagleBoard, the larger predecessor developed by Texas Instruments as an educational tool. The main processor on the board is a Sitara ARM Cortex-A8 processor running at 1Ghz and capable of running a full ARM based operating system (OS). The processor is also able to interface directly with low level communication protocols such as CAN, UART, SPI, and I2C. To meet our memory and speed requirements, a custom kernel was built with only the modules needed by our system. On top of this kernel, the Beagle Bone Black is running a ROS (Robot Operating System, see section 4.3 for more details) enabled Ubuntu ARM 14.04.1 LTS OS.

A new feature still being developed is the integration of DecaWave's DWM1000 module for relative distance measurements. Legacy components no longer utilized on the sensor board for mounting an XBee device are being used with a custom DWM1000 breakout board. The small breakout was designed to integrate the DWM1000 module into where the XBee device was originally mounted. Figure 4.4b shows an early prototype of the sensor board mounted to a Beagle Bone Black.

4.2.3 Power Board

The power board was design to enable safety, both for a person working near SUPERball and for the electronics, as well as conditioning input power to both a 5.5V and a 24V rail. The board was also designed with a minimal height profile allowing for larger batteries to be placed near the board. See section 4.1.2, to view the section which houses the power board. The main idea of safety is focused around operating the 100W BLDC motors, thus a two battery system was implemented. A small battery is used for starting the micro-controller boards but not capable of producing 24V needed by the motor, and a large battery is used during main operation of the MTR. The two batteries are a 160 milli-amp-hour 1-cell and a 3 amp-hour 6-cell lithium polymer batteries, named the back-up and the main respectively.

To enable the 24V power, multiple input conditions should be met and fed into an analog and-gate equivalent circuit. The input conditions are: a physical switch located on the MTR, a digital logic pin from the power board's micro-controller, power being applied by the back-

up battery, and a signal coming from a dedicated 8-bit micro-controller monitoring a pulsed wireless 2.4Ghz signal. If any one of these conditions go false, the entire 24V rail is disabled. There are also fuses on both the 24V and 5.5V line to protect all the micro-controller circuits from shorts. Figure 4.5 shows a basic connection diagram for the power lines.

The main processing unit on the power board is Microchip's 16-bit dspicPIC33ep128mc506 micro-controller. The wireless "kill switch" monitoring micro-controller is Microchip's 8-bit PIC12(L)F1571/2 micro-controller. This chip monitors a known pulse width being communicated by a Nordic Semiconductor nRF24L01 breakout board with antenna. The pulsed signal is sent by a hand held unit off the robot. When a shut off command is sent or the PIC12's watchdog timer is triggered from a loss in wireless signal, the logic signal sent from the PIC12 is turned to false disabling the 24V power rail. 5.5V power is either supplied by the back-up battery or the main battery using a custom boost or buck switching circuit, respectively. The 24V rail is supplied directly from the main 6-cell battery when all input logic is enabled. Figure 4.4c shows the power board.

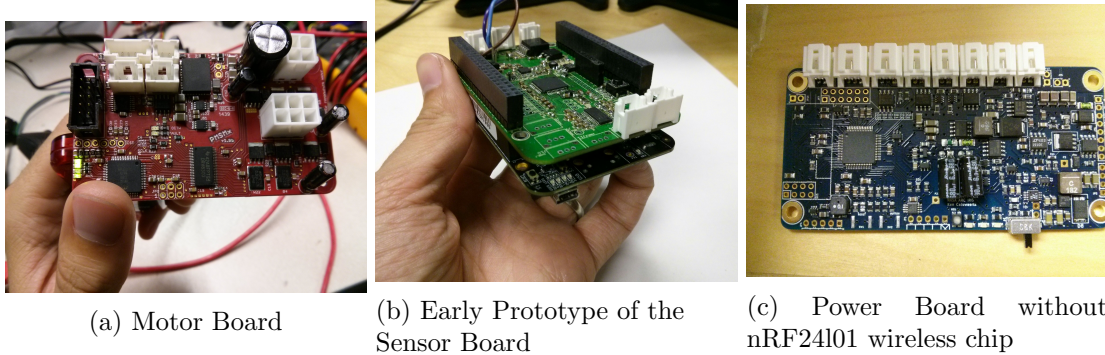


Figure 4.4: Pictures of each of the main micro-controller boards on an MTR.

4.3 Communication and Power

Communication on SUPERball was designed around a desire to have each rod of the tensegrity system unattached from any other part of the system. Two wireless protocols as well as a wired Controller Area Network, or CAN, bus were implemented. The two main wireless protocols are WiFi for main data communication and a 2.4GHz channel for wireless enabling/disabling of motor power for safety. Figure 4.5 shows how power and communication are connected for a single MTR and figure 4.6 shows the connections for SUPERball's wireless communications.

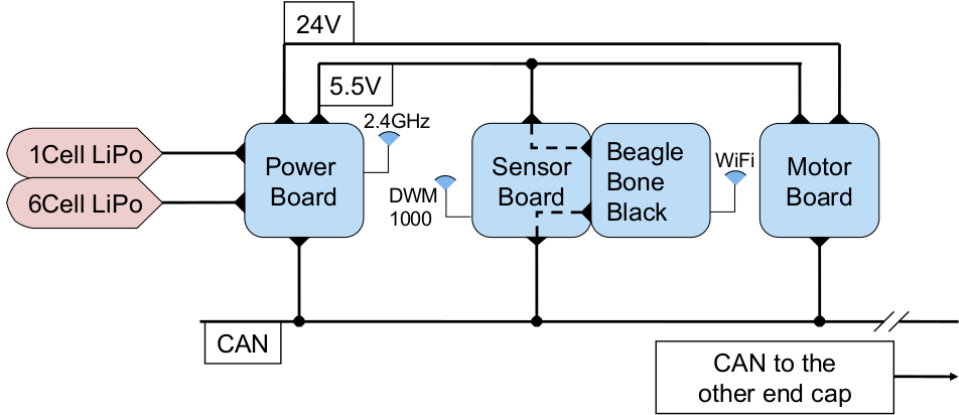


Figure 4.5: This is a connection diagram for power and communication for a MTR on SUPER-ball.

4.3.1 CAN Bus

A communication design was desired that would be robust, extensible, and work over long distances. A CAN bus fits these main requirements and was implemented to be the main communication between all controllers on a single rod. Since the CAN bus is a physical layer standard, a communication protocol is usually required to get a robust and extensible network. A widely accepted protocol that has been well tested and understood, is the CANOpen protocol [4]. CANOpen defines the addressing scheme, several small communication protocols and an application layer defined by a device profile. Some of the smaller communication protocols supported by CANOpen are device monitoring and communication between nodes, network management, and a simple transport layer for message processing. This open source protocol is freely distributed and has many open and closed source implementations. The CANOpen implementation used for SUPERball is the CANFestival project which focuses on implementing the basic protocol while maintaining a small code base and low computational load for embedded systems. Each micro-controller and Beagle Bone Black are able to run the entire CANFestival project code in less than $150\mu s$ under worst case scenarios. The physical layer CAN bus is running at $1Mbit/s$

4.3.2 WiFi and the Robot Operating System

The Robot Operating System, or ROS, is a collection of software to provide operating system functionality on a network linked computer cluster. Message-passing and packet management works agnostic to the network layer, allowing information to be passed from one ROS enabled node to any other ROS enabled node on a network. Figure 4.6 shows a basic representation of

how this message-passing works on the SUPERball ROS network.

As explained in section 4.2.2, enabling each rod is a ROS node was the driving reason to have at least one ARM based chip on every rod. Since the Beagle Bone Black is also on the CAN bus, it's main function is to sniff the CAN network and send new information out to the ROS network. This enables for near real time data analysis and for time stamped data logging on SUPERball.

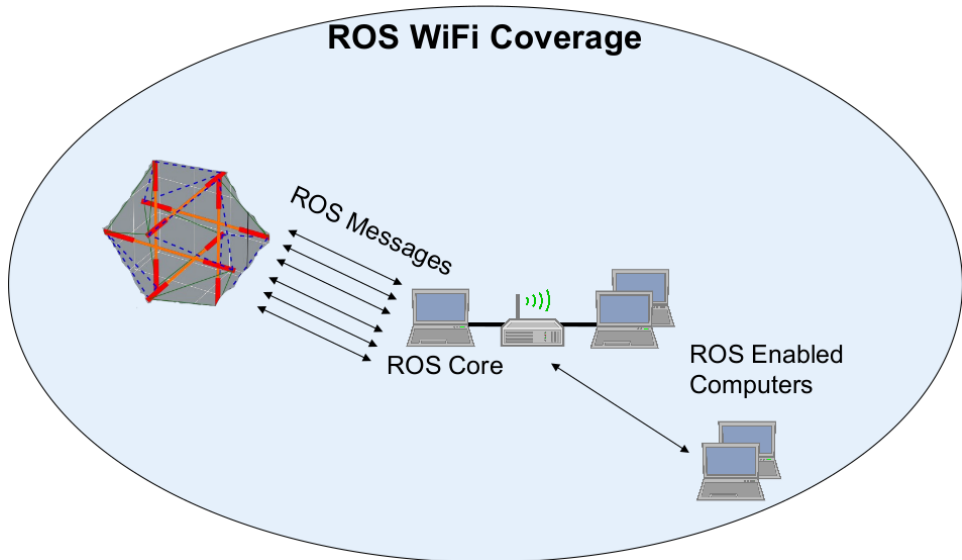


Figure 4.6: A simplified representation of how messages are passed within the SUPERball ROS network.

Chapter 5

Current and Future Work

5.1 SUPERball Current State

At this point, the first goal proposed in section 1.2 has been achieved. SUPERball is composed of twelve Modular Tensegrity Robots (MTR) attached as the ends of 6 rods connected in a icosahedron geometry, and may be seen in figure 3.1. Preliminary testing of the system, presented in the following sections, has shown many of the basic functions and features that will enable goals two and three. All data collected in this section was collected through the wireless ROS network with no extra sensors or equipment apart from what was designed into the system, explained in chapter 4.

5.1.1 Dynamic Torque Sensor Testing

This test was performed to demonstrate the force sensors' ability to capture data under dynamic motion. Figure 5.1 shows a plot of sensor data from one end cap whose motor is commanded in a square-wave position trajectory. The position trajectory had a period of 13 s, and oscillated between 10 rad and 15 rad of the output shaft measured before the gearbox, by the encoder. The trajectory of sensor torque values reasonably tracks the position square wave: the commanded position trajectory starts at 10 seconds and ends at 62 seconds, as does the sensed tension square wave. The overshoot on the torque sensor measurements is due to the system inertia and spring dynamics.

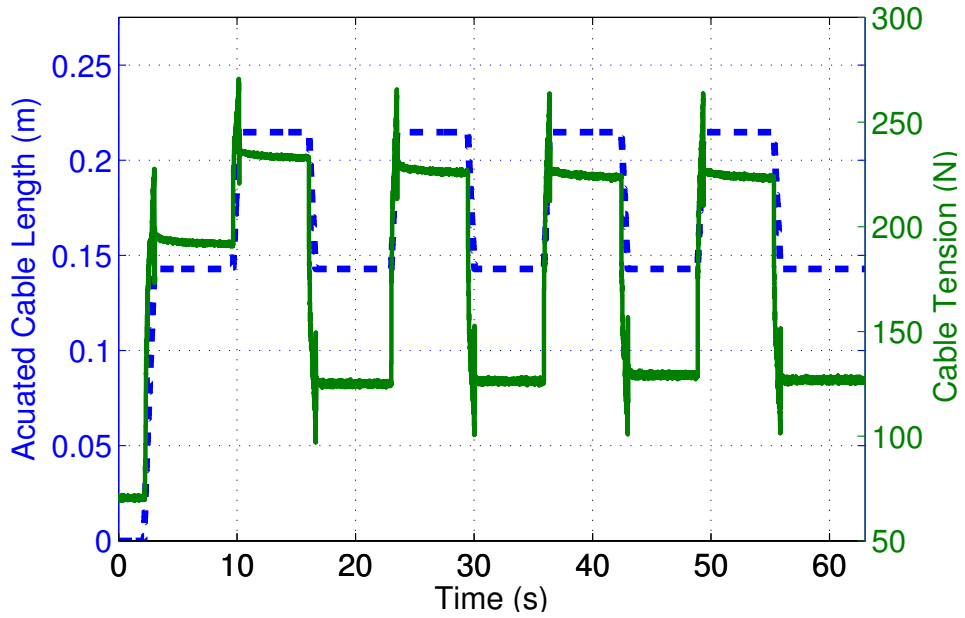


Figure 5.1: Motor mount torque sensor data and motor position data recorded during a square wave input position trajectory for a single motor. This plot shows measured tension from the sensor and cable length from motor encoder measurements as a function of time for this dynamic movement.

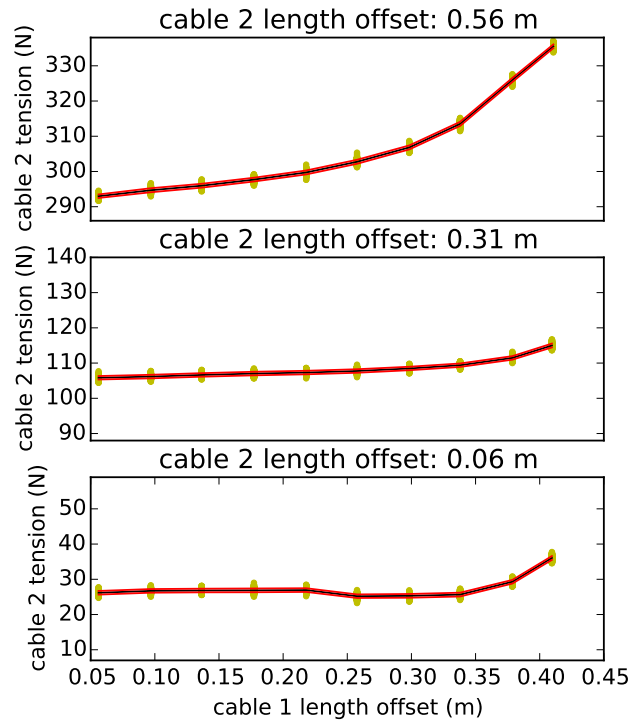
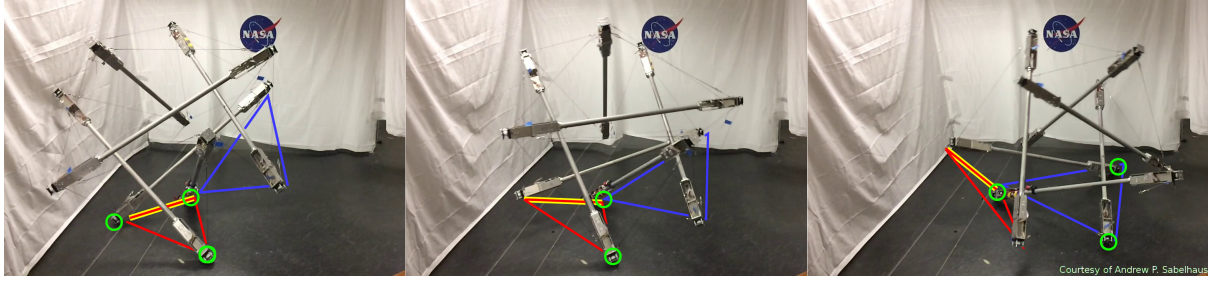


Figure 5.2: Global force redistribution test. Yellow marks are the means of roughly 5,000 tension sensor measurements of *cable 2* opposite that which is actuated (*cable 1*.) The black line shows the linear interpolation between points, with the red boundary as standard deviation. The pretension in the sensed cable is adjusted in each test, showing measurement sequences at increasing pretensions.



Courtesy of Andrew P. Sabelhaus

Figure 5.3: SUPERball performing a single face-change movement, from one equilateral triangular face to another. The robot begins with all MTRs of the red triangle touching the ground. Then, SUPERball retracts the yellow-highlighted cable on the red triangle, inducing movement. Frame 2 shows SUPERball halfway through the movement with only two points of contact on the ground. Finally, frame 3 shows SUPERball at the end, with all 3 points of the blue triangle in ground contact.

5.1.2 Global Force Redistribution Sensor Testing

A test was performed to validate the distribution of tension throughout the system, and to show that all sensors can work in conjunction simultaneously. Figure 5.2 shows tension readings from a different motor-mount torque sensor on the opposite side of SUPERball (Cable 2) from a cable which is being retracted (Cable 1.) Cable 2 was not actively actuated during each test. For each plot in Figure 5.2, the actuated cable was retracted with various step inputs marked in the figure. Each data point in this figure (yellow) was collected by averaging data from the sensor board for a total of 5 seconds at 1 kHz, after waiting 2 seconds after the step input actuation to avoid dynamic effects. These tests were done with different levels of pretension on the sensed cable: this pretension was adjusted by changing the length of the sensed cable. Though the lower-pretension tests show smaller changes in readings, the higher pretensions show increasing readings which demonstrate the ability to sense forces throughout the tension network in pseudo-equilibrium states, as well as SUPERball’s passive force redistribution properties.

5.1.3 Basic Locomotion

Using a basic step input to a single motor, SUPERball can perform a simple transition from one face of the icosahedron to another. Figure 5.3 shows a test where a motor retracts a cable, inducing a flop. The idea of this type of simple transition is to deform the base equilateral triangle such that the center of mass ”moves” over the triangle’s edge. The robot becomes unstable and gravity pulls the system over. The momentum of the system then rolls the robot through the adjacent isosceles triangle to the next equilateral triangle. In this test, the motor retraction was preset and experimentally derived earlier.

5.2 Future Work

5.2.1 Open Loop Locomotion Control

For clarity, open loop used here is open in regards to the locomotion system's ability to change robotic motor inputs based on environmental sensing. Work presented in [11] shows through simulation that a tensegrity system like SUPERball can achieve a rolling gait by deforming the triangle currently in contact with the ground. Though SUPERball is not fully actuated (all 24 external cables are attached to motors), a derivative of this work may be able to be applied to SUPERball. Leveraging the experimental results from section 5.1.3, SUPERball can achieve open loop locomotion quite easily with the addition of detecting which face of the robot is on the ground. To achieve this ground detection, I propose to use the IMU modules on each sensor board to detect earth's gravity field and/or ground contacts when a rod contacts the ground. Using a basic machine learning technique, like k-nearest neighbor, may enable successful classification of where the ground is in relation to the robot.

5.2.2 Closed Loop Locomotion Control

There has been preliminary results done by [5] which demonstrates a tensegrity robot sensing different enviromental terrains. This shows promise that a tensegrity robot may sense changes in terrain without the need for extra sensors. If a similar technique can be achieved on SUPERball in a real-time manor, then the open loop gait pattern used from 5.2.1 can be altered to better locomote over the sensed terrain. This new locomotion gait may either be hand tuned parameters or learned behavior.

Bibliography

- [1] Adrian Agogino, Vytas SunSpiral, and David Atkinson. Super Ball Bot - structures for planetary landing and exploration. *NASA Innovative Advanced Concepts (NIAC) Program, Final Report*, 2013.
- [2] T. Bliss, J. Werly, T. Iwasaki, and H. Bart-Smith. Experimental validation of robust resonance entrainment for CPG-controlled tensegrity structures. *IEEE Transactions On Control Systems Technology*, 21:666–678, 2012.
- [3] V. Bohm and K. Zimmermann. Vibration-driven mobile robots based on single actuated tensegrity structures. In *ICRA*, pages 5475–5480, May 2013.
- [4] H Boterenbrood. Canopen high-level protocol for can-bus. *Nikhef, Amsterdam*, 2000.
- [5] Jeroen Burms, Ken Caluwaerts, and Joni Dambre. Online unsupervised terrain classification for a compliant tensegrity robot using a mixture of echo state networks. In *Robotics and Automation (ICRA), 2015 IEEE International Conference on*, pages 4252–4257. IEEE, 2015.
- [6] Ken Caluwaerts, Jérémie Despraz, Atil İşcen, Andrew P. Sabelhaus, Jonathan Bruce, Benjamin Schrauwen, and Vytas SunSpiral. Design and control of compliant tensegrity robots through simulation and hardware validation. *Journal of The Royal Society Interface*, 11(98), 2014.
- [7] Ken Caluwaerts, Michiel D’Haene, David Verstraeten, and Benjamin Schrauwen. Locomotion without a brain: physical reservoir computing in tensegrity structures. *Artificial Life*, 19(1):35–66, 2013.
- [8] Etienne Fest, Kristina Shea, Ian F C Smith, and M Asce. Active Tensegrity Structure. *October*, 130(October):1454–1465, 2004.

- [9] R. B. Fuller. *Synergetics: Explorations in the Geometry of Thinking*. Scribner, January 1975.
- [10] A. Graells Rovira and J. M. Mirats-Tur. Control and simulation of a tensegrity-based mobile robot. *Robotics and Autonomous Systems*, 57(5):526–535, May 2009.
- [11] Atil Iscen, Adrian Agogino, Vytas SunSpiral, and Kagan Tumer. Flop and roll: Learning robust goal-directed locomotion for a tensegrity robot. In *Intelligent Robots and Systems (IROS 2014), 2014 IEEE/RSJ International Conference on*, pages 2236–2243. IEEE, 2014.
- [12] Mark Khazanov, Julian Jocque, and John Rieffel. Developing morphological computation in tensegrity robots for controllable actuation. In *GECCO*, pages 1049–1052, 2014.
- [13] Kyunam Kim, Adrian K. Agogino, Deaho Moon, Laqshya Taneja, Aliakbar Toghyan, Borna Dehghani, Vytas SunSpiral, and Alice M. Agogino. Rapid prototyping design and control of tensegrity soft robot for locomotion. In *To Appear in ROBIO*, 2014.
- [14] Y. Koizumi, M. Shibata, and S. Hirai. Rolling tensegrity driven by pneumatic soft actuators. In *ICRA*, pages 1988–1993, 2012.
- [15] RD Lorenz. Huygens probe impact dynamics. *ESA Journal*, 18:93–117, 1994.
- [16] Pavlo Manovi. Pmsm. <https://github.com/FrauBluher/PMSM>, 2014.
- [17] J.M. Mirats-Tur and J. Camps. A three-dof actuated robot. *Robotics Automation Magazine, IEEE*, 18(3):96–103, Sept 2011.
- [18] C. Paul, F. J. Valero-Cuevas, and H. Lipson. Design and control of tensegrity robots for locomotion. *IEEE Transactions on Robotics*, 22(5), October 2006.
- [19] M. Shibata, F. Saijyo, and S. Hirai. Crawling by body deformation of tensegrity structure robots. In *ICRA*, pages 4375 –4380, may 2009.
- [20] R. E. Skelton and M. C. De Oliveira. *Tensegrity Systems*. Springer, 2009 edition, June 2009.
- [21] R. E. Skelton and M. C. De Oliveira. *Tensegrity Systems*. Springer, 2009 edition, June 2009.

- [22] Robert Skelton. Dynamics and control of tensegrity systems. In H. Ulbrich and W. Gnther, editors, *IUTAM Symposium on Vibration Control of Nonlinear Mechanisms and Structures*, volume 130 of *Solid Mechanics and its Applications*, pages 309–318. Springer Netherlands, 2005.
- [23] Kenneth Snelson. Continuous tension, discontinuous compression structures. United States patent 3169611, February 1965.
- [24] Cornel Sultan, Martin Corless, and Robert Skelton. Tensegrity flight simulator. *Journal of Guidance, Control, and Dynamics*, 23(6):1055–1064, 2000.
- [25] Vytas SunSpiral, George Gorospe, Jonathan Bruce, Atil Iscen, George Korbel, Sophie Milam, Adrian Agogino, and David Atkinson. Tensegrity based probes for planetary exploration: Entry, descent and landing (EDL) and surface mobility analysis. In *10th International Planetary Probe Workshop (IPPW)*, July 2013.
- [26] Gunnar Tibert. *Deployable Tensegrity Structures for Space Applications*. PhD thesis, Royal Institute of Technology, 2002.
- [27] N. Wang, K. Naruse, D. Stamenović, J. J. Fredberg, S. M. Mijailovich, I. M. Tolić-Nørrelykke, T. Polte, R. Mannix, and D. E. Ingber. Mechanical behavior in living cells consistent with the tensegrity model. *PNAS*, 98(14):7765–7770, Jul 2001.
- [28] Ning Wang, Jessica D Tytell, and Donald E Ingber. Mechanotransduction at a distance: Mechanically coupling the extracellular matrix with the nucleus. *Nature Reviews Molecular Cell Biology*, 10(1):75–82, 2009.